

**MODELLING OF CMOS BASED INTERLEAVED  
PN JUNCTION OPTICAL PHASE SHIFTERS**

**ABDURRAHMAN JAVID SHAIKH**

**UNIVERSITI SAINS MALAYSIA**

**2019**

**MODELLING OF CMOS BASED INTERLEAVED PN JUNCTION OPTICAL  
PHASE SHIFTERS**

**by**

**ABDURRAHMAN JAVID SHAIKH**

**Thesis submitted in fulfilment of the  
requirements for the degree of  
Doctor of Philosophy**

**January 2019**

## **DEDICATION**

This work is dedicated:

- to the most influential person in my life, my ever-loving mother (Badrunnisa), who sacrificed everything in her today for me to have everything in my tomorrow.
- to the loving memories of my father (Javid Ahmed), whom I wish I could thank in person for all the motivation, enthusiasm, and immense knowledge given to me to start this journey.

I will never be able to express my gratitude.

## ACKNOWLEDGEMENT

For many of us, PhD journey is like our first ever solo trekking experience on some remote unfamiliar terrain. We may be feeling solitary throughout this expedition, but there are many without whom we would not be even able to start this journey. Those who would encourage and equip us for this task, those who would shout “watch out!” for our every wrong move, those who would pull us up before continuing back on their own paths, and those who were not there with us on our journey but their prayers and well wishes were. I may not be able to thank them all but I acknowledge those who made their mark.

Foremost, I am grateful to Allah (SWT) who enabled me to take up this task and successfully complete it. He chose this path for me to make me understand many things which I would never be able to comprehend otherwise. I am deeply indebted to my supervisors Dr. Mohamed Fauzi Packeer Mohamed and Prof. Dr. Othman Bin Sidek for their guidance and incessant support throughout my studies. I would like to express my deep gratitude to the school management especially our former and incumbent deans Prof. Ir. Dr. Mohd Rizal Bin Arshad and Prof. Ir. Dr. Mohd Fadzil Bin Ain, respectively, for their continuous support. I would also like to sincerely thank the honourable vice-chancellor, NED University (Prof. Dr. Sarosh H. Lodi) and the dean of faculty of electrical and computer engineering, NED University (Prof. Dr. Saad Ahmed Qazi) for their incessant support and trust in me.

During our graduate studies it is our family who suffers the most, therefore, I am deeply thankful to my family for having the patience with me for having taken this challenge which decreased the amount of time I could spend with them. Especially, I would like to express my gratitude to my siblings Abdullah Javid, Sadyah Asad,

Javeryah Javid, Maryah Abdul Qadir and Sumyyah Faisal for supporting me in the way I would never be able to repay. I am very much thankful to my wife (Humna) for her constant support, consideration and patience with me during my hectic PhD journey. Acknowledgements are also due on me for my daughters (Raifah and Tooba) who inspired me to work harder in their own ways.

Partial scholarship under faculty development programme of NED University is hereby acknowledged. Acknowledgement will not be complete should the following names are not mentioned who assisted me time to time during the course of my PhD studies: Gul Munir Ujjan, Mufti Abdul Qadir, Abu Baha Habashi, Abul Hassan Quadri, Abdul Ghani Abro, Zakir Ahmed, Dr. Shahid Iqbal, Ubaidullah, Cik Siti Norlaila Binti Ahmad, Nishat Akhtar, Ashar Ahmed, Tariq Adnan, Norshah Rizal, and Dr. Faisal Nadeem Khan. I thank you all for your support.

## TABLE OF CONTENTS

	<b>Page</b>
<b>ACKNOWLEDGEMENT</b>	<b>ii</b>
<b>TABLE OF CONTENTS</b>	<b>iv</b>
<b>LIST OF TABLES</b>	<b>viii</b>
<b>LIST OF FIGURES</b>	<b>ix</b>
<b>LIST OF ABBREVIATIONS</b>	<b>xvi</b>
<b>ABSTRAK</b>	<b>xviii</b>
<b>ABSTRACT</b>	<b>xx</b>
<b>CHAPTER ONE: INTRODUCTION</b>	
1.1 Background	1
1.2 Short Reach Optical Interconnects and CMOS Photonics	3
1.3 Problem Statement	6
1.4 Research Objectives	8
1.5 Contributions of This Work	9
1.6 Organization of the Thesis	11
<b>CHAPTER TWO: LITERATURE REVIEW</b>	
2.1 Phase and Intensity Modulation	14
2.2 Modulator Figures of Merit (FOMs)	17
2.2.1 Device Level FOMs	17
2.2.2 System Level FOMs	20
2.3 Modulation Mechanisms in Silicon	23
2.3.1 Electro-Optic Effects	23

2.3.2	Plasma Dispersion Effect	25
2.3.3	Thermo-Optic Effect	26
2.3.4	Acousto-Optic Effect	27
2.4	Plasma Dispersion Modulators: Modes of Operation	27
2.5	Depletion Mode PDE Modulators: Junction Topologies	32
2.6	Modelling of Optical Phase Modulators	35
2.6.1	Full Analytical Approach	36
2.6.2	Semi-Analytical Approach	38
2.6.3	Full 3D Numerical Approach	40
2.7	Modelling Physics and Methods	41
2.7.1	Optical Simulations: The FDFD Method	42
2.7.2	Device Simulations: The Drift-Diffusion & Poisson's Equations	43
2.7.3	The Finite-Difference-Time-Domain (FDTD) Method	48
2.8	Design of the Single Mode SOI Rib Waveguides	49
2.8.1	The Single Mode Condition	50
2.9	Discussion	53
2.10	Summary	56

## **CHAPTER THREE: METHODOLOGY**

3.1	Introduction	58
3.2	Overall Analysis and Design Workflow	59
3.3	Stage 1: The Passive Submicron Rib Waveguide Analysis and Design	63
3.3.1	The Single Mode Condition	64
3.3.2	The Optical Mode Confinement Factor and Nature of the Mode	65

3.3.3	The Zero Birefringence (ZBR) Condition	66
3.3.4	Parameter Sweeps and Data Generation	67
3.3.5	Convergence Testing	74
3.4	Stage 2: Three Dimensional Plasma Dispersion Simulations of PN-Junction Modulators	75
3.4.1	The Electronic Structure of Interleaved Phase Modulator	76
3.4.2	Non-uniform Finite Element Mesh	78
3.4.3	Incorporation of Semiconductor Material Models	81
3.4.4	Parameter Sweeps and Data Generation	85
3.4.5	Convergence Testing	90
3.5	Stage 3: Three-Dimensional (3D) Optoelectronic Simulations	93
3.5.1	Calculation of Free Carrier Index and Free Carrier Absorption	93
3.5.2	Evaluation of Modulator's Performance Metrics	96
3.5.3	Simulation Setup, Parameter Sweeps and Data Generation	97
3.5.4	Convergence Testing	104
3.6	Obtaining Mathematical Models	105
3.7	Summary	106

## **CHAPTER FOUR: RESULTS AND DISCUSSIONS**

4.1	Introduction	107
4.2	Analysis and Design of Passive Optical Waveguide	107
4.2.1	The Single Mode Conditions	108
4.2.2	Control of Mode Confinement Factor ( $\Gamma$ )	111
4.2.3	The Zero Birefringence (ZBR) Conditions	114
4.2.4	Model Validation	119



4.3	Predictive Model for Modulation Efficiency (ME)	122
4.3.1	The Predictive Model	127
4.4	Predictive Model for Junction Capacitance ( $C_j$ )	130
4.4.1	The Predictive Model	137
4.5	Predictive Model for Phase Shifter Bandwidth ( $f_{3dB}$ )	139
4.5.1	The Predictive Model	149
4.6	Model Comparison with Published Works	151
4.6.1	Modulation Efficiency	151
4.6.2	Junction Capacitance	154
4.6.3	Phase Shifter Bandwidth	157
4.6.4	Pitch Length for Maximum Per-Unit Length Speed ( $L_{MPUS}$ )	160
4.7	Summary	161

## **CHAPTER FIVE: CONCLUSION AND FUTURE WORKS**

5.1	Conclusion	163
5.2	Future Works	164

<b>REFERENCES</b>	166
-------------------	-----

## **APPENDICES**

Appendix A: Model Fitting Coefficients

Appendix B: Derivation of Pitch Length for Maximum Per-Unit Length Speed ( $L_{MPUS}$ )

## **LIST OF PUBLICATIONS**

## LIST OF TABLES

		<b>Page</b>
Table 2.1	Performance metrics of various plasma dispersion effect based modulators fabricated and reported in literature.	31
Table 2.2	Summary of the key modelling and simulation attempts in the literature for the plasma dispersion based optical modulators	54
Table 3.1	Default values of the PML boundary parameters used in this thesis	75
Table 3.2	Fundamental parameters, their typical values, correction models and values of the model parameters used in the numerical analysis.	82
Table 3.3	Advanced parameters of the semiconductor material (Si), their typical values, correction models and values of the model parameters used in the numerical analysis.	84
Table 3.4	Modulator device parameters and their values simulated in this study.	86
Table 3.5	Waveguide geometric parameters and their values simulated in this study.	87
Table 3.6	Parameters that affect the simulation results and their values used in the simulations, where the convergence in the results have already been achieved.	105
Table 4.1	Values of the fitting coefficients ('a' to 'e') against various rib heights, used in the mathematical model of predicting ZBR condition (equation (4.12) & (4.13))	118
Table 4.2	Modulation Efficiency: Several designs fabricated in silicon foundries and reported in various literature.	152
Table 4.3	Junction Capacitance: Several designs fabricated in silicon foundries and reported in the various literature.	155
Table 4.4	Phase Shifter Bandwidth: Several designs fabricated in silicon foundries and reported in various literature.	158

## LIST OF FIGURES

		<b>Page</b>
Figure 1.1	A typical route an information packet would pursue from and to end-user devices. Not shown in this figure are the local area network connections where optical alternatives are available.	2
Figure 1.2	Typical building blocks of an optical link (Martin, 2015)	4
Figure 1.3	Growth in photonic device integration density for a decade future trend (Hochberg et al. , 2010)	5
Figure 2.1	Commonly used passive structures, incorporating the active phase modulators to achieve intensity modulation. (A) Mach-Zehnder Interferometer based modulator incorporating phase shifters on either or both arms (Akiyama et al., 2014) , (B) Passive Ring-Resonator (RR) structure, (C) RR based modulator incorporating interleaved junction phase shifter (Xiao et al., 2012).	16
Figure 2.2	Transmission spectra of ring resonator based depletion mode modulator for various applied voltage (Pantouvaki et al., 2015)	19
Figure 2.3	The modes of operation of silicon PN junction phase modulators. (A) Carrier accumulation, (B) Carrier injection, and (C) Carrier depletion. (Reed et al., 2010). The white arrows show injection of majority carriers.	28
Figure 2.4	Typical junction topologies employed to achieve depletion-mode plasma dispersion modulators. (A) vertical junction, (B) horizontal junction, and (C) interleaved junction.	34
Figure 2.5	Two dimensional (collapsed in height) equivalent of the three-dimensional interleaved PN junctions optical phase shifter (Perez-Galacho et al., 2014).	38
Figure 2.6	Full analytical optoelectronic modelling approach for interleaved PN junction phase shifters	38
Figure 2.7	The three-dimensional interleaved PN junctions optical phase shifter where the modelling approach involves analytical solution of device characteristics together with numerical mode solving (Perez-Galacho et al., 2014).	39
Figure 2.8	Semi-analytical optoelectronic modelling approach for interleaved PN junction phase shifters (Perez-Galacho et al., 2014).	39
Figure 2.9	The three-dimensional interleaved PN junctions optical phase	41

shifter where the modelling approach involves 3D numerical solution of device characteristics together with numerical mode solving (Perez-Galacho et al., 2014).

Figure 2.10	Full 3D optoelectronic modelling approach for interleaved PN junction phase shifters (Perez-Galacho et al., 2014).	41
Figure 2.11	The three dimensional Yee cell. The locations where the three components of electric and magnetic fields are evaluated are also mentioned.	49
Figure 2.12	(A) Cross-sectional view of a typical rib waveguide structure. 'W' represents the final rib width while 'H' represents total rib height, including slab height 'h' and etch depth 'D'. (B) Scanning Electron Microscope image of a typical slanted-sidewall submicron silicon rib waveguide (after	50
Figure 3.1	Three dimensional perspective view of the interleaved PN junction rib waveguide phase modulator modelled in this thesis.	59
Figure 3.2	Overall analysis and design workflow of an integrated waveguide phase modulator. The overall workflow includes three discrete and sequentially interlinked stages.	61
Figure 3.3	Cross-sectional view of a typical rib waveguide structure. 'W' represents the rib width while 'H' represents total rib height, including slab height 'h' and etch depth 'D'.	64
Figure 3.4	Mode field profile under the rib and its respective intensity variation with respect to the vertical (right hand side to the mode profile) and horizontal (below the mode profile) directions through the mode peaks (a) fundamental mode (b) first-order vertical mode (c) first-order horizontal mode. A single mode waveguide would only support fundamental mode profile.	65
Figure 3.5	Flowchart of the core routine performing: (i) parameter sweeps over waveguide dimensions, (ii) simulation mesh adjustments, (iii) simulation parameters adjustments, and (iv) sub-routine calls to evaluate single mode performance of the waveguide, confinement and nature of the supported fundamental mode.	69
Figure 3.6	The <i>Single Mode Tester</i> subroutine, developed in this thesis to identify whether the structural dimensions set by the <i>core</i> routine represent a single mode waveguide or not.	70
Figure 3.7	The Mode Field Evaluator (MFT) subroutine, developed in this thesis to identify whether the modes supported by a structure exhibit the field profile of the fundamental mode or	73

	not. This algorithm of evaluation the mode field profile is based on subsection 3.3.1.	
Figure 3.8	Transformation of an electronically inactive/passive silicon waveguide structure (A) to an electronically active silicon waveguide modulator device (B), enabled by careful doping and device design.	76
Figure 3.9	Orthogonal views (A, C, and D) and the perspective view (B) of the device to be analyzed.	77
Figure 3.10	The perspective view of the modulator devices studied in the thesis, showing dopant densities as well as the grid in various regions of the device structure.	79
Figure 3.11	Orthogonal views of the modulator device structure: (A) Cross-sectional view (XZ-axis), (B) Top-down view (XY-axis), Bottom-up view (XY-Axis), and the (D) Side view (YZ-Axis). Variation in dopant density is clearly visible as variation in the device colour scheme. The associated grid size variation is also evident – smaller around the junction region and higher dopant densities, and larger (comparatively) in the region with relatively little or no variation in the dopant densities.	80
Figure 3.12	Flowchart of the core routine performing: (i) device parameters sweeps over fixed waveguide geometric parameters, (ii) simulation mesh adjustments, (iii) simulation parameters adjustments, and (iv) sub-routine calls to evaluate device slab resistance and junction capacitance.	88
Figure 3.13	Flowchart of the subroutine calculating the junction capacitance of the waveguide modulators studied in this thesis.	90
Figure 3.14	Convergence tests' results and the chosen values of the simulation parameters for steady state analysis of the phase modulator. The cross markers in each of the graphs show the value of the divider used in the simulations.	92
Figure 3.15	The magnitude of the variation of the FCI (A) and FCA (B) versus free electron density. The free hole-density is taken as a parameter in both the graphs.	95
Figure 3.16	Flowchart of the core routine: (i) loading each of the spatial charge profile as per the device parameters sweeps over fixed waveguide geometric parameters, (ii) calculating the FCI and FCA, (iii) performing simulation mesh adjustments, (iv) simulation parameters adjustments, and (v) sub-routine calls to evaluate device steady state and dynamic behaviours.	98
Figure 3.17	Top view of the waveguide modulator structure showing the	100

	locations of the active waveguide segment, result monitors and mode source. The light grey/white region is the passive waveguide generated by the FDTD <i>core</i> routine, and the segment between vertical lines ‘1’ and ‘2’ is the electronically active region where the charge distribution had been calculated in stage 2 and converted into the refractive index distribution in this stage.	
Figure 3.18	Flowchart of the part of the subroutine called by the FDTD’s <i>core</i> routine to calculate the steady state phase variations ( $\Delta\Phi_{ss}$ ) to finally calculate the modulation efficiency.	101
Figure 3.19	Flowchart of the code evaluating the transient behaviour (transition time and modulation bandwidth) of the waveguide phase modulator.	102
Figure 4.1	Comparison of the fundamental TE mode and multimode boundary obtained from this thesis (the solid curves) with the work of Dai and Sheng (square/diamond/triangle symbols), and Chan (solid circles). The curves show that the results obtained from this work are in good agreement with the other reported works (Dai et al., 2007, Seong Phun a al., 2005).	109
Figure 4.2	The single mode region bounded by three boundary conditions representing only those dimensions which supported fundamental mode only.	111
Figure 4.3	The single mode region and related variation in the single mode boundary conditions with respect to the minimum mode confinement factor. The global upper boundary systematically disappears as the slope of the upper boundary decreases with increase values of $\Gamma_{min}$ .	113
Figure 4.4	Graph (D vs W) of waveguide dimensions fulfilling the zero birefringence condition. Rib height is taken as the parameter in each graph with: $0.70 \mu\text{m} \leq H \leq 1.0 \mu\text{m}$ (A), $0.40 \mu\text{m} \leq H \leq 0.7 \mu\text{m}$ (B), and $0.25 \mu\text{m} \leq H \leq 0.4 \mu\text{m}$ (C).	116
Figure 4.5	Graph (D vs W) of waveguide dimensions fulfilling the zero birefringence condition for all the rib height (H).	117
Figure 4.6	Model validation with the simulated data for various confinement factors. The markers show the simulated results while the lines show the respective model. The models are in good agreement with the results.	120
Figure 4.7	Model validation for predicting ZBR condition with the simulated data for various rib heights. The markers show the simulated results while the lines show the respective model. The models are in good agreement with the results. The RMS	121

	error never exceeded 3.5% for any case.	
Figure 4.8	Model validation for the fitting coefficients ('a' and 'b') used to predict the ZBR condition with the data given in Table 4.1 for various rib heights. The markers show the data point from the table while the lines show the respective model. The models are in good agreement with the results. The calculated RMS error of about 5% is noted.	121
Figure 4.9	Modulation Efficiency ( $V_{\pi}L_{\pi}$ ) of the simulated phase shifter designs with respect to variations in the device design parameters. Geometric parameters: H=220 nm, W=400 nm, h=80 nm.	123
Figure 4.10	Modulation Efficiency ( $V_{\pi}L_{\pi}$ ) of the simulated phase shifter designs with respect to variations in the device design parameters. Geometric parameters: H=220 nm, W=400 nm, h=105 nm, t=500 nm.	126
Figure 4.11	Modulation Efficiency ( $V_{\pi}L_{\pi}$ ) of the simulated phase shifter designs with respect to variations in the device design parameters. Geometric parameters: H=220 nm, W=500 nm, h=103 nm, t=500 nm.	126
Figure 4.12	Modulation Efficiency ( $V_{\pi}L_{\pi}$ ) of the simulated phase shifter designs with respect to variations in the device design parameters. The geometric parameters were fixed at H=400 nm, W=400 nm, h=80 nm, t=500 nm.	127
Figure 4.13	Definition of $L_s$ . It is the sum of $L_1$ and $L_2$ .	128
Figure 4.14	Junction capacitance ( $C_j$ ) of the simulated phase shifter designs with respect to variations in the device design parameters. Geometric parameters: H=220 nm, W=400 nm, h=70 nm.	132
Figure 4.15	Junction capacitance per unit length versus the applied reverse bias potential for various impurity concentration. The higher the dopant concentration the larger the slope of the CV-curves.	133
Figure 4.16	Junction capacitance ( $C_j$ ) of the simulated phase shifter designs with respect to variations in the device design parameters. Geometric parameters: H=220 nm, W=400 nm, h=105 nm, t=500 nm.	134
Figure 4.17	Junction capacitance ( $C_j$ ) of the simulated phase shifter designs with respect to variations in the device design parameters. Geometric parameters: H=220 nm, W=500 nm, h=103 nm, t=500 nm.	135

Figure 4.18	Junction capacitance (CJ) of the simulated phase shifter designs with respect to variations in the device design parameters. Geometric parameters: H=400 nm, W=400 nm, h=80 nm, t=500 nm.	136
Figure 4.19	Bandwidth per unit length (GHz/ $\mu\text{m}$ ) of the simulated phase shifter designs with respect to variations in the device design parameters. Geometric parameters: H=220 nm, W=400 nm, h=70 nm.	142
Figure 4.20	Cross-sectional areas faced by the free carriers in the rib region of the waveguide ( $\Delta A_{\text{rib}}$ ) and by the free carriers in the slab region ( $\Delta A_{\text{slab}}$ ). Increasing finger length ( $L_P$ or $L_N$ ) means increasing channel cross-sectional area for the carriers in the slab region, decreasing $R_{\text{slab}}$ . Continuous increase in the finger length may eventually result in $R_{\text{slab}} < R_{\text{rib}}$ . ' $y_P$ ' is the depletion region depth in P-type material and ' $y_N$ ' is the depletion region depth in the N-type material.	144
Figure 4.21	Bandwidth per unit length (GHz/ $\mu\text{m}$ ) of the simulated phase shifter designs with respect to variations in the device design parameters. Geometric parameters: H=220 nm, W=400 nm, h=105 nm, t=500 nm.	146
Figure 4.22	Bandwidth per unit length (GHz/ $\mu\text{m}$ ) of the simulated phase shifter designs with respect to variations in the device design parameters. Geometric parameters: H=220 nm, W=500 nm, h=103 nm, t=500 nm.	147
Figure 4.23	Bandwidth per unit length (GHz/ $\mu\text{m}$ ) of the simulated phase shifter designs with respect to variations in the device design parameters. Geometric parameters: H=400 nm, W=400 nm, h=80 nm, t=500 nm.	148
Figure 4.24	Comparison of the model predicted modulation efficiency with several designs actually fabricated in foundries and reported in the literature. Design 1 (Zieball et al., 2011); Design 2 (Xiao et al., 2012); Design 3 (Pantouvaki et al., 2013); Design 4 – 7 (Yu et al., 2012).	153
Figure 4.25	Comparison of the model predicted junction capacitance (per unit length) with several designs actually fabricated in foundries and reported in the literature. Design 1 (Ziebell et al., 2011); Design 2 (Xiao et al., 2012); Design 3 (Xu et al., 2012); Design 4 (Pantouvaki et al., 2013); Design 5 (Yu et al., 2012).	155
Figure 4.26	Comparison of the model predicted modulation bandwidth with several designs actually fabricated in foundries and reported in the literature. Design 1 (Xiao et al., 2012); Design	158



2 (Xu et al., 2012); Design 3 – 6 (Yu et al., 2013).

Figure 4.27 The Per-unit length bandwidth of the optical phase shifters reported in (Pantouvaki et al., 2013) versus the pitch length of the interleaved designs (dashed curve). The solid curve is the model fit of the data (reciprocal quadratic model), for extrapolation and estimation of  $L_{MPUS}$ , which came out to be 1.643 from graphs as opposed to 1.727 calculated from the formula derived in Appendix B (equation). Less than 5% error in estimation. Data for comparison taken from: design # 4 – 6 of Table 4.4 161

## LIST OF ABBREVIATIONS

AI	Artificial Intelligence
AOE	Acousto-Optic Effect
BPM	Beam Propagation Method
BR	Bit Rate
BW	Bandwidth
CJ	Junction Capacitance
CMOS	Complementary Metal Oxide Semiconductor
DD	Drift-Diffusion
EB	Exa-Byte
EDA	Electronic Design Automation
EIM	Effective Index Method
EO	Electro-Optic
ER	Extinction Ratio
FD	Finite Difference
FDE	Finite Difference Eigenmode
FDFD	Finite Difference Frequency Domain
FDTD	Finite Difference Time Domain
FEM	Finite Element Mesh
FKE	Franz-Keldysh Effect
FOM	Figures Of Merit
Gbps	Giga bits per second
GT/s	Giga Transfer per second
IL	Insertion Loss

IoT	Internet of Things
ME	Modulation Efficiency
MOS	Metal Oxide Semiconductor
MZI	Mach-Zehnder Interferometer
MZM	Mach-Zehnder Modulator
OBW	Optical Bandwidth
PDE	Plasma Dispersion Effect
PIN	P-type/Intrinsic/N-type
pm/V	pico-meter per Volt
ROADM	Reconfigurable Optical Add/Drop Multiplexer
RR	Ring Resonator
RRM	Ring Resonator Modulator
SM	Single Mode
SMC	Single Mode Condition
SOI	Silicon-On-Insulator
WDM	Wavelength Division Multiplexing
ZBR	Zero BiRefringence

# PEMODELAN CMOS BERDASARKAN PENGANJAK FASA OPTIK PERSIMPANGAN PN ANTARA LEMBARAN

## ABSTRAK

Prestasi saling-hubung optik bergantung kepada dasar reka bentuk pemodulat optik. Prestasi pemodulat-pemodulat ini sebahagian besarnya dipengaruhi oleh penganjak fasa optik terbenam. Antara beberapa topologi, penganjak fasa persimpangan antara lembaran mod susutan adalah yang paling berpotensi kerana berkelajuan tinggi yang berkaitan dengan operasi mod susutan dan kecekapan modulatan tinggi yang berkaitan dengan struktur persimpangan antara lembaran. Oleh kerana kerumitan struktur topologi antara lembaran, prestasi penganjak fasa bergantung kepada beberapa parameter reka bentuk. Selain itu, pertukaran ganti yang rumit wujud di antara pelbagai metrik prestasi berkenaan dengan pembolehkan reka bentuk ini. Untuk reka bentuk pemodulat yang berdaya maju, pengoptimuman adalah perlu yang memerlukan model-model ramalan prestasi. Dalam sorotan kajian, hanya penyelidikan berangka awal yang telah dijalankan untuk memahami tingkah laku topologi yang begitu berpotensi, itu pun, dengan banyak andaian-andaian yang tidak realistik dipermudahkan. Walau bagaimanapun, penganjak fasa persimpangan antara lembaran, memerlukan pemodelan tiga dimensi (3D) yang rapi untuk penerangan sebenar prestasi pemodulat. Model-model ramalan matematik 3D sedemikian tidak terdapat di dalam sorotan kajian. Dalam tesis ini simulasi elektronik optik tiga dimensi, menggabungkan model-model berasaskan fizik dan model-model pembetulan yang mencukupi, telah dilakukan untuk mendapatkan keputusan berangka yang rapi. Aliran kerja keseluruhan dibahagikan dalam tiga peringkat. Alat-alat piawaian industri daripada *Lumerical Inc.* berdasarkan *Finite-Difference-*

*Frequency-Domain (Lumerical MODE Solutions), Finite-Element-Modelling (Lumerical DEVICE TCAD), dan Finite-Difference-Time-Domain (Lumerical FDTD Solutions)* telah digunakan untuk pemodelan pandu gelombang (peringkat 1), peranti (peringkat 2) dan penganjak fasa (peringkat 3). Model-model ramalan yang tak linear kemudiannya diperolehi dengan melaksanakan prosedur-prosedur penyesuaian lengkung secara teliti dengan menggunakan MATLAB 2015b. Untuk pertama kalinya, garis-garis panduan matematik yang komprehensif untuk reka bentuk pasif rusuk pandu gelombang submikron telah dicadangkan bersama-sama dengan model-model ramalan matematik untuk kecekapan modulatan, kapasitans per unit panjang, dan lebar jalur bagi penganjak fasa optik. Ketepatan model-model telah dibandingkan terhadap reka bentuk yang telah difabrikasikan di foundri. Dicatatkan kesilapan anggaran adalah lebih kurang 7 % atau kurang untuk kesemua model-model yang telah dicadangkan. Model-model sedemikian akan membolehkan pengoptimuman aplikasi yang khusus untuk silikon submikron penganjak fasa optik persimpangan PN antara lembaran.

# **MODELLING OF CMOS BASED INTERLEAVED PN JUNCTION OPTICAL PHASE SHIFTERS**

## **ABSTRACT**

The performance of an optical interconnect depends on the underlying optical modulator design. Performance of these modulators is largely influenced by the embedded optical phase shifters. Among several topologies, depletion-mode interleaved junction phase shifters are most promising because of the high speed associated with depletion mode of operation and high modulation efficiency associated with interleaved junction structure. Due to structural complexity of interleaved topology, the phase shifter performance depends on several design parameters. Also, intricate trade-offs exist among various performance metrics with respect to these design variables. For viable modulator design, optimization is necessary which requires performance predictive models. In the literature, only preliminary numerical research has been pursued to understand the behaviour of such a promising topology, that too, with many simplifying unrealistic assumptions. Interleaved junction phase shifters, however, require rigorous three-dimensional (3D) modelling for true description of the modulator performance. Such 3D mathematical predictive models are absent in the literature. In this thesis three dimensional optoelectronic simulations, incorporating physics-based models and adequate correction models, have been performed to obtain rigorous numerical results. The overall workflow is divided in three stages. Industry standard tools from Lumerical Inc. based on Finite-Difference-Frequency-Domain (Lumerical MODE Solutions), Finite-Element-Modelling (Lumerical DEVICE TCAD), and Finite-Difference-Time-Domain (Lumerical FDTD Solutions) have been used for waveguide (stage 1),

device (stage 2) and phase shifter (stage 3) performance modelling respectively. Nonlinear predictive models are then obtained by pursuing careful, stage-wise curve fitting procedures using MATLAB 2015b. For the first time, comprehensive mathematical guidelines for the passive design of submicron rib waveguides have been proposed along with mathematical predictive models for modulation efficiency, capacitance per unit length, and bandwidth of the optical phase shifters. The accuracy of the models have been compared against the foundry fabricated designs. An estimation error of about 7% or below was noted for all the proposed models. Such models would enable application specific optimization of submicron silicon interleaved PN-junction optical phase shifters.

# CHAPTER ONE

## INTRODUCTION

### 1.1 Background

With an estimated rate of 212 petabytes per day, big data is expected to reach a staggering volume of 403 exabytes (EBs) in 2021 which would represent about 30% of the total data stored in data centres (Cisco, 2018). In its previous report, Cisco estimated appreciably smaller growth of big data contribution to total data on the data centres (Cisco, 2016), indicating ever increasing acceptance of the paradigm specially in enterprise segment. Increasing connectivity and data creation due to internet of things (IoT), opened entirely new domains of applications and flow of data to the servers is expected to increase manifold (Duranton et al., 2017). By 2021, the magnitude of data stored, driven by IoT, has been forecasted to increase four-folds reaching about 24 EBs per day (Cisco, 2018). In 2016 alone, these technologies contributed to enormous 19 EBs of global data centre traffic per day; forecasted to increase more than three times to reach about 58 EB per day by 2021 (Cisco, 2018). Fruitful realization of these pervasive, high traffic and computationally intense systems calls for massively parallel processing capabilities together with efficient data transport mechanisms (Rumley et al., 2017). For efficient data transport and parallel processing, interconnects of various scales play the vital role (Zhou et al., 2018a).

As for data transmission, congestion at any stage from client to server (and back) due to bottlenecks in information processing machines like routers and switches and due to limited interconnect bandwidth adds to communication delays. Figure 1.1 shows a typical path an information packet would take from an end-user device to some remote processing station (data centre). The long haul optical media provide



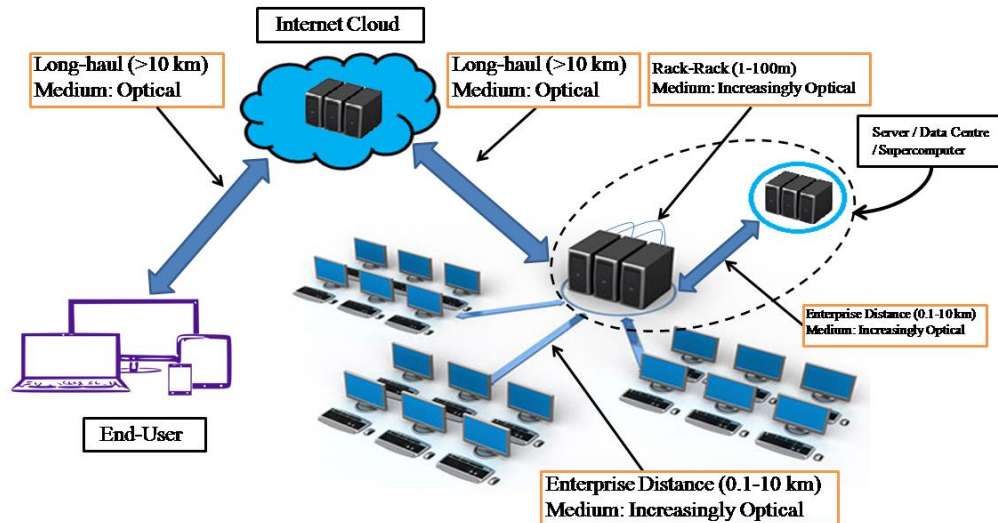


Figure 1.1: A typical route an information packet would pursue from and to end-user devices. Not shown in this figure are the local area network connections where optical alternatives are available.

extremely wide bandwidth connectivity enabling high capacity data transmission over longer distance.

Moving down the scale, the inter-data centre interconnects have become optical in nature to support higher transmission capacity (Benner et al., 2005). At further lower scale (intra-centre: rack-to-rack etc.), interconnects are becoming increasingly optical and a complete transition from metallic Ethernet connections to optical seems only imminent. The data centre traffic is maximum at this scale and amounts to about 75% of the total data centre bound traffic (Cisco, 2018, Krause Perin et al., 2018). Interconnects of scales smaller than rack-to-rack are the ones residing inside processing machines. These include board-to-board, chip-to-chip, and on-chip interconnects which are all metallic in nature (short reach interconnects). Traffic congestion must be avoided at this scale to enhance overall system performance.

As for data processing, multi-core processors together with distributed computing architectures are widespread and are more viable for their cost effectiveness

and scalability. Nevertheless, these parallel architectures, together with promising performance enhancements in short reach (intra-machine) interconnects, did not result in performance growth of, for example, 20 most powerful supercomputers since mid-2013, as it had been prior to that (Rumley et al., 2017). The performance growth slowed down due to bottlenecks at the metallic on-board and on-chip scale interconnects. One of the major contribution to this bottleneck emerges due to the hierarchal nature of the current interconnect implementation. Implementing optical interconnects, on the other hand, at this scale makes it possible to avoid whole of the hierarchy of interconnections at small scale (device to chip, chip to board, board to backplane, backplane to cable) and tremendously increase transmission capacity, improving overall system performance (Miller et al., 1997) by orders of magnitude.

To date, short reach interconnects are metallic for their technological maturity, cost-effectiveness and reliability. However, metallic interconnects are low in transmission capacity as space-division-multiplexing is the only multiplexing mechanism available (Zhou et al., 2018a). They are also high in power consumption as they require capacitive charging before information is transmitted through them (Miller, 2009, Miller et al., 1997). The optical counterparts are being actively researched now. The possibility of wavelength-division multiplexing in optical interconnects together with extremely high carrier frequency results in per lane transmission capacity of several orders of magnitude larger as compared to the metallic interconnects (Zhou et al., 2018a).

## **1.2 Short Reach Optical Interconnects and CMOS Photonics**

The active search for communication solutions in optical domain has been triggered by arguably a single main factor: demand of processing exploding amount of data at faster speeds (Stucchi et al., 2013). Optical interconnect links answer these

demands, typical building blocks of which are shown in Figure 1.2 (Martin, 2015). The link contains a source (typically a laser (Duan et al., 2015, Gallet et al., 2017, Valicourt et al., 2018)), optical couplers (Romero-García et al., 2015), optical modulators (Baba et al., 2013, Baba et al., 2015, Thomson et al., 2012), light guiding/routing structures (Heck et al., 2014) and photo-detectors (Huang et al., 2015, Lee, 2016). Continuous-wave high frequency laser beam is coupled into the optical link and the passive light guiding structures (waveguides, Y-branches, add/drop filters etc.) guide these high frequency optical fields throughout the link. The continuous wave optical beam is converted into optical pulses (representing the data to be transmitted) by means of optical modulators. The modulator in this optical link is an active device communicating with the non-optical domain. Therefore, performance of this device affects the overall performance of optical interconnects; the faster the modulator encodes the data on optical carrier wave, the higher the link capacity.

Complementary-Metal-Oxide-Semiconductor (CMOS) compatible photonic design requires material and process compatibility with already existing CMOS fabrication technology. The optical device must comply with CMOS processing steps, processing temperatures, and all other materials present in a CMOS wafer. If the material used to design the photonic device needs, for example, high annealing temperatures ( $\sim 1000\text{ }^{\circ}\text{C}$ ); the material and hence the device is not CMOS compatible as such high temperatures will affect the metallic structures. In CMOS-compatible designs, such requirements inhibit the use of other materials which are commonly used

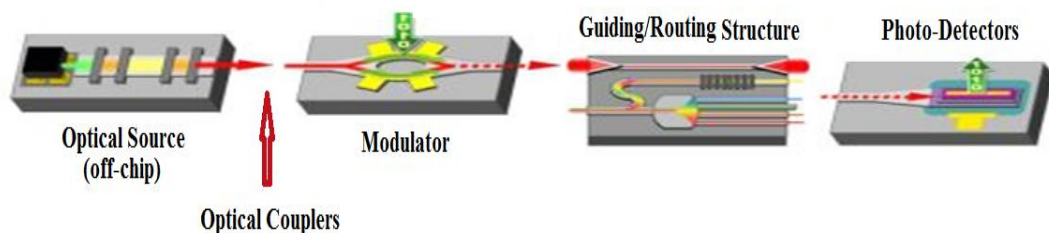


Figure 1.2: Typical building blocks of an optical link (Martin, 2015).

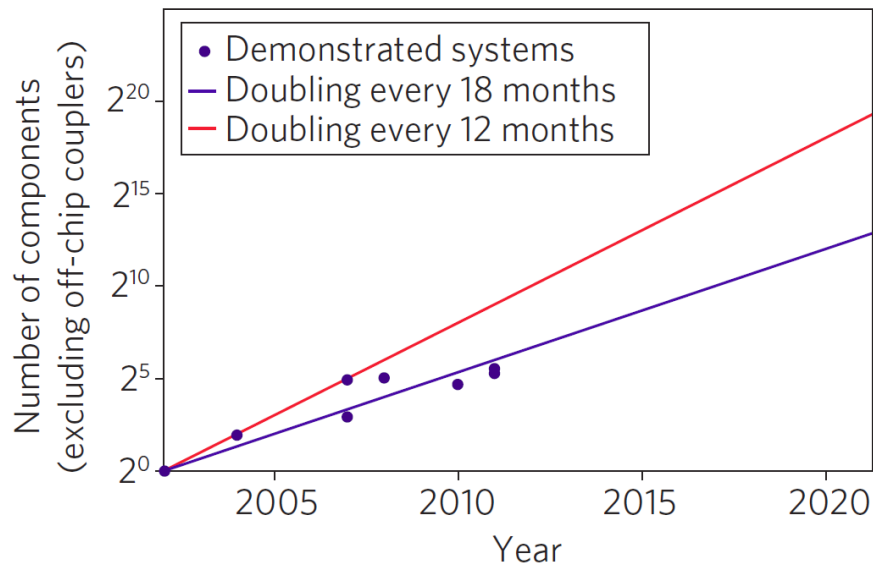


Figure 1.3: Growth in photonic device integration density for a decade future trend (Hochberg et al., 2010).

in optical systems (like Lithium-Niobate and III-V materials) (Gunn, 2006). The photonic device should also demonstrated CMOS circuit compatibility in terms of drive voltages (Ding et al., 2012a, Gill et al., 2009, Gunn, 2006, Tsybeskov et al., 2009). With decreasing device dimensions to achieve high modulation speeds, the drive voltages must also be reduced to avoid material breakdown due to high electric fields.

Silicon is not only CMOS-compatible but also became material of choice for optical interconnects because of its favourable material properties like high refractive index (~3.47 at 1550 nm), high thermal conductivity (1.56W/cm/K), and extremely low intrinsic absorption loss at technologically important wavelengths (1310 nm and 1550 nm). The optical material properties were augmented by the extensive processing knowledge and highly mature fabrication infrastructure for monolithic optoelectronic integration at fibre optic wavelengths (Izhaky et al., 2006, Tsybeskov et al., 2009). Critical dimension control of contemporary fabrication facilities enables precise control of waveguide dimensions. High refractive index of silicon together with

cladding of low-index ( $\sim 1.45$ ) enable strong confinement of light. This high index contrast, in turn, enables photonic device design using ultrasmall cross section waveguides for various applications (Bauters et al., 2013, Cardenas et al., 2009, Grillot et al., 2006, Heck et al., 2014). Waveguide devices now have feature sizes of few tens of nanometres as compared to several hundred nanometres in 1990s (Dai et al., 2007, Leuthold et al., 2010, Seong Phun et al., 2005). Tight optical confinement of electromagnetic fields at much higher frequency of operation along with high bandwidth capabilities, silicon based optical interconnects may result in less interference and higher device integration densities (Miller, 2009, Miller et al., 1997). The growth in the silicon photonic device integration density has followed a pace comparable to Moore's law for electronics with doubling in the number of integrated devices every eighteen months (Figure 1.3) (Hochberg et al., 2010). Hence, silicon photonics has plenty of opportunity and promise to realize optical interconnects for next generation hyperscale computing applications. The only CMOS-compatible design requirement remains is maintaining low drive voltages, typically  $< 1$  V (Gill et al., 2009).

### **1.3 Problem Statement**

Silicon photonics is promising platform for short reach optical interconnects for its suitable material properties, device and process knowledge, compatibility with mature CMOS processes, possibility of monolithic photonic-electronic integration, and cost effectiveness. However, due to its centrosymmetric structure, silicon lacks the favourable linear electro-optic effects (Frigerio et al., 2015, Soref et al., 1987a). This leads to free carrier plasma dispersion effect as the only viable mechanism for modulation in silicon. Particularly, the depletion mode silicon optical modulators have been studied extensively in recent years for their high speed and low power

consumption as compared to injection mode PIN or accumulation mode metal-oxide-semiconductor (MOS) structures respectively (Reed Graham et al., 2014, Reed et al., 2010). Nevertheless, depletion mode modulators suffer greatly with very small modulation efficiency, resulting in large device footprints, inconsistent with chip-scale photonics. For this, novel interleaved PN-junction based phase shifter structures were proposed (Li et al., 2009). This topology resulted in modulation efficiency comparable to injection mode modulators, however, is a compromise between efficiency and bandwidth.

Performance of optical modulators directly affects the interconnect performance (Reed et al., 2010). The challenge is to develop compact and low power consumption optical modulators (Frigerio et al., 2015). The performance of the phase modulator depends on many design variables including structural parameters as well as doping and operating voltages. Limitations on cross-sectional dimensions of the device are normally derived from the requirements on the waveguide to support the fundamental mode only and confine a prescribed fraction of optical mode. Moreover, the device should be birefringence free. Comprehensive submicron waveguide design guidelines to address these requirements are absent in the literature. Mathematical design guidelines to achieve single mode condition, ensure achievement of minimum mode confinement, and zero-birefringence condition have been proposed for submicron rib waveguides based on silicon-on-insulator material system for the first time in this thesis.

Each of the several design variables may influence all the performance metrics of the phase shifter and hence the intensity modulator. Typical phase modulator performance metrics include modulation efficiency, capacitance per unit length, and modulation bandwidth (Reed, 2014). These metrics manifest intricate interdependence

with respect to the design variables. Increasing dopant concentration or device cross-sectional dimensions, for example, will increase modulation efficiency but capacitance per unit length of the device will also increase. Increased capacitance is linked with higher power consumption (Reed, 2014) and, therefore, is not suitable. On the other hand, modulation bandwidth increases with increasing doping and decreases with decreasing cross-sectional dimensions of device. Such trade-offs necessitate design optimization for a particular application. Prior to optimization, however, performance predictive models are required. There have been attempts in the literature to propose graphical representation of the interleaved phase shifter behaviour, but none provided mathematical predictive models. Moreover, the numerical analysis performed in the literature made non-realistic assumptions which made the analysis relevant only for device understanding at fundamental level. For realistic mathematical models, however, full vectorial and three dimensional analysis, incorporating all applicable physical models, is required. Such three-dimensional mathematical predictive models are absent in the literature. These models will enable device optimization. In this thesis, predictive models of key figures of merit have been proposed for the first time.

#### **1.4 Research Objectives**

Due to absence of performance predictive models in the literature, this thesis aims at proposing three dimensional (3D) mathematical predictive models for key figures of merit of submicron optical phase modulators based on depletion mode interleaved PN-junctions. Providing comprehensive guidelines for the passive design of submicron rib waveguides is also one of the aims of this work. This thesis proceeds to achieve following research objectives;

- 1) To investigate and identify the 3D numerical modelling procedure which may be adopted to simulate and analyse CMOS-compatible depletion mode interleaved

PN-junction optical phase shifters with submicron dimensions.

- 2) To propose mathematical design guidelines, based on rigorous numerical analysis, to achieve single mode condition, ensure achievement of a minimum mode confinement, and for simultaneous achievement of zero-birefringence and single mode condition in submicron SOI rib waveguides.
- 3) To generate ample amount of valid numeric data for modulation efficiency, modulation bandwidth and junction-capacitance of CMOS-compatible depletion mode interleaved PN-junction optical phase shifters with systematic variation in design variables.
- 4) To propose mathematical predictive models for modulation efficiency, junction capacitance per unit length, and bandwidth of CMOS-compatible depletion mode interleaved PN-junction optical phase shifters with submicron dimensions.

## 1.5 Contributions of This Work

The contributions of this thesis are significant which not only include the predictive models and design guidelines but also include the algorithms used to achieve the proposed models and guidelines. These algorithms are novel and may be used for future similar studies. Specifically, contributions of this work include;

- 1) **Algorithms for numerical analysis of passive waveguide:** Algorithms devised and adopted (chapter 3) after literature review for numerical analysis of the single mode conditions and identification of the fundamental mode profile (subsection 3.3.1 and subsection 3.3.4) are novel and may be used to automate similar analyses in other applications. With little modifications, the algorithms can be applied to any type of waveguide structure (rib, strip, slot etc.).
- 2) **Algorithms for 3D optoelectronic modelling of interleaved junction phase shifters:** Due to carrier-density variations in all the three space dimensions, the



simulations and modelling required for the interleaved structure must be three-dimensional. The complexity of the problem increases nonlinearly with respect to space dimensions. Algorithms have been devised to automate the whole simulation process and reliable data generation to study modulation efficiency, energy-per-bit and bandwidth of the interleaved pn-junction phase shifter structure.

- 3) **Comprehensive guidelines for passive SOI rib waveguide design:** For reliable performance of waveguide based optical modulators, single mode condition must be ensured. At the same time, the waveguide must confine satisfactory amount of mode power in the rib region for the mode to be guided. Mode confinement also affect all the modulator performance metrics. Finally, it is highly desirable that the designed waveguides be birefringence free. Mathematical design guidelines, based on rigorous numerical analysis, have been proposed to achieve single mode condition, ensure achievement of a minimum mode confinement, and for simultaneous achievement of zero-birefringence and single mode condition in submicron SOI rib waveguides.
- 4) **Predictive models for CMOS-compatible submicron interleaved PN-junction based phase shifters:** Mathematical predictive models, after rigorous 3D simulation and meticulous modelling procedures, have been proposed for three of the key device level figures of merit. These models include: (i) modulation efficiency, which directly affects the device footprint, power consumption, and speed limitations due to electrode sizes, (ii) capacitance-per-unit length, which directly affects energy consumed in producing a “bit” of information, modulation speed and efficiency, and finally, (iii) phase shifter’s speed. All these models take into account all the design variables based on device’s geometric dimensions as well as doping densities and their dimensional extent. Since the dopant density-

type (P-type and N-type) and their respective proportions affect the device performance, a significant contribution of this thesis is to include symmetric as well as asymmetric designs in the study and modelling process. Moreover, the models also take into account the effects of optical mode confinement for the first time along with 3D modelling.

- 5) **Enabling custom optimization tasks:** The models enable generation of reliable performance data for systematic combinations of all the affecting design variables. This structured data can be used to define cost functions for a specific application. The structured cost function data may then be used in two ways. Firstly, to fit the cost functions against all the design parameters by systematic curve-fitting followed by linear optimization procedures to find the best design; or secondly, to optimize the cost function directly using advanced artificial intelligence (AI) based computational methods. The data generated can be huge in volume for higher reliability.

## 1.6 Organization of the Thesis

This thesis adopts more of a formal organization bearing five chapters (Introduction, Literature Review, Methodology, Results and Discussions, Conclusion and Future Works). After setting the premise and the context of the work in this chapter, the thesis proceeds with an in depth review of the literature (chapter 2). Starting from basis of phase modulation and achieving intensity modulation therefrom (section 2.1), the chapter presents a detailed review of the figures of merit, in which performance of optical modulators are compared (section 2.2), along with their interrelation. The chapter then reviews the physical limitations of silicon as a material of choice for photonic modulation, justifying plasma dispersion effect as the most viable mechanism (section 2.3). The modes of operation of the plasma dispersion

effect based phase modulators (section 2.4) and the junction topologies to achieve plasma dispersion in depletion-mode modulators (section 2.5) have then been presented. The justification to use the depletion-mode phase shifters and the interleaved junction structure along with their modelling implications are vividly presented. The investigation for the modelling procedure is then pursued in the literature (section 2.6), majorly from the last two decades, to explore the available modelling techniques and trends adopted to simulate optoelectronic problems. Effort is made to figure out the most rigorous and methodologically valid technique applicable to the interleaved structure. This section forms the basis to all the algorithms presented in chapter 3. Modelling physics and mathematical techniques associated with the identified modelling approach is then described succinctly (section 2.7). Works pertaining to the design of the single mode, high confinement factor, birefringence free, passive rib waveguide structure based on the silicon-on-insulator material systems is then reviewed next (section 2.8). A discussion offering critical review to analyse the research gap is given in section 2.9 and summary is presented in section 2.10.

Chapter 3 (Methodology) starts with the introduction (section 3.1) and the overall analysis and design workflow (section 3.2). Every stage (passive waveguide design, plasma dispersion study, optoelectronic analysis) under the overall workflow has been dealt with separately in detail (sections 3.3, 3.4, and 3.5). These sections contain the algorithms devised in this thesis to simulate the active and passive devices. Chapter 4 (Results and Discussions) begins with the analysis of passive rib waveguides and proposes the mathematical design guidelines (section 4.2) as stipulated in the second objective of this work. The chapter then moves on to propose the three predictive models for modulation efficiency, junction capacitance and phase shifter

bandwidth in sections 4.3, 4.4, and 4.5 respectively. The proposed predictive models are then compared with the already published results based on foundry fabricated designs for model validation (section 4.6). The thesis is then concluded in chapter 5, where future studies that can be pursued have also been proposed.

## CHAPTER TWO

### LITERATURE REVIEW

#### 2.1 Phase and Intensity Modulation

Optical phase modulators have the capability to change the refractive index of the material and hence change wavelength and bring about phase shift in an optical wave propagating through the material (based on the voltage applied or current supplied). This capability although significant is not enough alone to generate optical pulses (logical 1s or 0s). Therefore, phase modulators, almost always, are embedded in a passive optical structure to achieve intensity modulation, resulting in optical ‘1s’ and ‘0s’ based on electrical ‘1s’ and ‘0s’ (Chang et al., 2017, Li et al., 2017, Zhou et al., 2018b). The configurations which are generally used to achieve intensity modulation are based on passive: (i) Mach-Zehnder Interferometric (MZI) configuration (Baba et al., 2015, Cao et al., 2013, Ding et al., 2012a, Ding et al., 2012b, Dong et al., 2012, Goykhman et al., 2013, Green et al., 2007, Liao et al., 2005, Marris-Morini et al., 2013, Thomson et al., 2012, Tu et al., 2013, Xiao et al., 2013, Xu et al., 2014, Xu et al., 2011, Xu et al., 2012, Yang et al., 2015, Zhou et al., 2016), (ii) ring resonator (RR) based configuration (Akiyama et al., 2014, Baba et al., 2013, Hu et al., 2012, Jayatilika et al., 2013, Marris-Morini et al., 2013, Pantouvaki et al., 2013, Rosenberg et al., 2012, Xiao et al., 2012), (iii) ring-assisted MZI structures (Cardenas et al., 2013, Gutierrez et al., 2012, Wang et al., 2016, Zhang et al., 2016), or (iv) coupled resonator structures (Li et al., 2008, Xu, 2009, Yu et al., 2014, Zhou et al., 2018b).

A propagating electromagnetic wave can be described in terms of its propagating electric and magnetic fields respectively as follows (Reed, 2004);

$$E = E_0 e^{j(kz \pm \omega t)} \quad (2.1)$$

$$H = H_0 e^{j(kz \pm \omega t)} \quad (2.2)$$

where,  $E_0$  and  $H_0$  are the electric and magnetic phasor amplitudes,  $t$  is the time (sec),  $z$  is the direction of propagation,  $\omega$  is the wave-frequency (rad/sec) and  $k$  is the wavenumber (rad/m). The phase ( $\phi$ ) of this propagating wave contains the wavenumber ( $k$ ):

$$\phi = (kz \pm \omega t) \quad (2.3)$$

where,  $k$  is related to wavelength ( $\lambda$ ) as follows;

$$k = \frac{2\pi}{\lambda} \quad (2.4)$$

The wavenumber in free space ( $k_0$ ) and the wavenumber in a medium other than free space ( $k$ ) are related by refractive index of the medium ( $n$ ) (Agrawal, 1997):

$$k = nk_0 \quad (2.5)$$

By virtue of free carrier plasma dispersion effect, refractive index of the material is modulated which, in turn, modulates the phase of the optical wave.

The two most common passive structures used to embed the phase modulators to achieve intensity modulation are shown in Figure 2.1. Figure 2.1A shows the typical MZI based modulator structure (MZM) in a push-pull configuration (Akiyama et al., 2014), while Figure 2.1B shows a passive ring-resonator, and Figure 2.1C shows the RR-based modulator structure (RRM) incorporating interleaved junction phase shifter (Xiao et al., 2012).

In MZM, the phase shifter(s) are located at either or both of the arms of the MZI structure. The arm lengths can be symmetric or asymmetric. The optical input splits equally (ideally) in the two arms maintaining the same relative phase. The idea

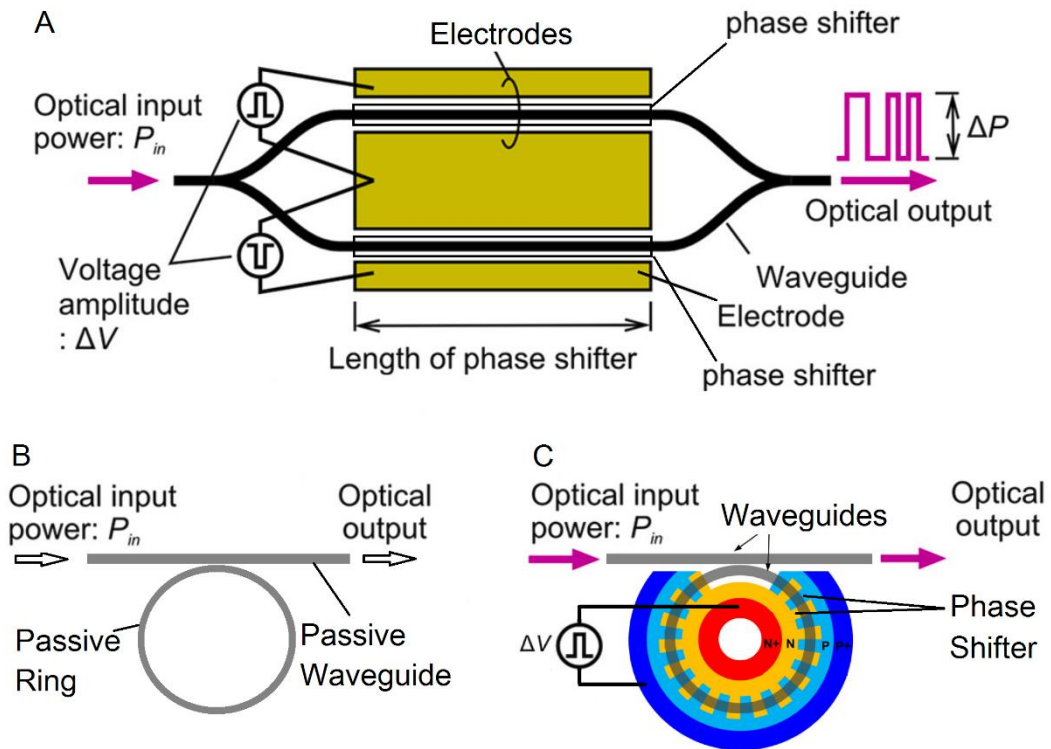


Figure 2.1: Commonly used passive structures, incorporating the active phase modulators to achieve intensity modulation. (A) Mach-Zehnder Interferometer based modulator incorporating phase shifters on either or both arms (Akiyama et al., 2014), (B) Passive Ring-Resonator (RR) structure, (C) RR based modulator incorporating interleaved junction phase shifter (Xiao et al., 2012).

is to achieve phase difference between the modes travelling in the two arms of the MZI before the modes recombine at the output end. The phase shift is achieved by applying electrical signal on the terminal electrodes of the phase modulator or by removing it. The phase difference should be  $180^\circ$ , if an optical ‘0’ is required. Otherwise, for an optical ‘1’, there should be no phase difference in the two propagating modes at the combining end of the structure. For an optical ‘0’, the phase shifter length must be long enough (at a given applied voltage) to achieve the  $180^\circ$  relative phase shift.

In the RRM (Figure 2.1C), the phase modulator is located on the ring of the passive structure (Figure 2.1B), hence the effective index change happens on the ring with changing applied electrical signal. This may cause the resonant structure to either enter the resonance condition, causing optical ‘0’ at the output, or leave the resonance

condition, causing optical ‘1’ at the output. In RRM, other parameters like coupling coefficient and ring quality factor also play important role in deciding extinction ratio and speed of the modulator device.

## **2.2 Modulator Figures of Merit (FOMs)**

Design requirements on electro-optic modulators are generally imposed by the application for which the modulators are being designed. For few applications, device modulation speed and power consumption may be more important than device footprint, for example, in high-speed optical interconnects. For other applications device footprint may not be as important as insertion loss and modulation depth or extinction ratio, for example, in case of telecommunication devices. The design requirements are further complicated by the intricate interplay of the modulator performance metrics. The metrics include many terminologies (Pantouvaki et al., 2013, Reed Graham et al., 2014, Reed et al., 2010): Phase efficiency, modulation efficiency, capacitance-per-unit-length, energy-per-bit, modulation bandwidth (BW), bit rate (BR), optical loss, extinction ratio, device footprint, insertion loss, and optical bandwidth. The performance metrics mentioned above, may be broadly categorized as the device level figures of merit (FOMs) or the system level FOMs. At system level, the application area directs about the crucial set of system level FOMs to focus on. This set also helps on deciding the intensity modulation scheme to be used. In this section, it is intended to categorize and summarize all the FOMs pertaining to optical modulators and to justify the study of the three device level FOMs.

### **2.2.1 Device Level FOMs**

The device level FOMs pertain to phase modulator / phase shifter and include modulation efficiency ( $V_{\pi}L_{\pi}$ ), modulation bandwidth, capacitance-per-unit-length, and optical loss (Reed Graham et al., 2014). Phase efficiency, although not always the



same, may always be related to the modulation efficiency. Specifically, phase efficiency relates to the change in effective index per unit voltage applied (or current supplied) on the phase modulator terminals. For MZMs, the modulation efficiency relates to the length of the phase shifter required (in cm) to achieve  $180^\circ$  phase change at the output of the modulator ( $L_\pi$ ) if the modulator is operated by 1V signal (Rasigade et al., 2011). In the plasma dispersion modulators (subsection 2.3.2 and section 2.4), the required length ( $L_\pi$ ) reduces if the applied voltage (or supplied current) is increased and is nonlinearly related to the applied stimulus (Ziebell et al., 2011). Therefore, the modulation efficiency is better represented by the product of  $L_\pi$  and the voltage at which the  $L_\pi$  is achieved ( $V_\pi$ ), i.e.,  $V_\pi L_\pi$  (measured in V.cm). For RRM, modulation efficiency is a measure of the resonant wavelength phase shift that occurs due to the effective index change in the ring per unit voltage (or current). Figure 2.2 (Pantouvaki et al., 2015) shows the transmission spectra of an RR-based depletion mode modulator for various applied voltages. The modulation efficiency shown here is at -1 V. Typically, modulation efficiency in an RRM is measured in resonance wavelength shift that occurs per unit voltage (pm/V). It is apparent from the Soref's formula (section 2.6.1) (Nedeljkovic et al., 2011, Soref et al., 1987a, Soref et al., 1987b) that the material index variation, thereby effective index change and hence resonant wavelength shift, is directly proportional to the change in free carrier density in the path of optical mode. For a fixed dopant concentration, the change in the free carrier concentration is directly proportional to the applied voltage (or supplied current) and the length of the phase shifter. Again, the change in carrier density is nonlinearly related to the applied voltage (supplied current), hence the modulation efficiency in the case of RRM can be represented by the voltage-shifter length product (V.cm) (Xiao et al., 2012).

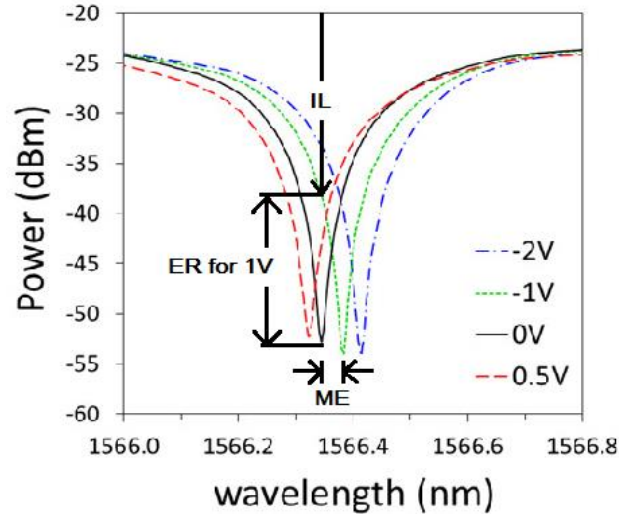


Figure 2.2: Transmission spectra of ring resonator based depletion mode modulator for various applied voltage (Pantouvaki et al., 2015).

The second device level FOM, capacitance-per-unit length, is linked with many other device level and system level FOMs (Pantouvaki et al., 2013). The effective junction capacitance of a phase shifter is proportional to the optical mode confinement of the passive structure. The higher the mode confinement, the larger the junction capacitance. Similarly, the modulation efficiency is also directly proportional to the mode confinement. The junction capacitance is also affected by dopant density, so is the modulation efficiency. The higher the dopant density, the higher the junction capacitance and modulation efficiency. Therefore, modulation efficiency and effective junction capacitance per unit length are directly related. Apart from its relation with the modulation efficiency, the total junction capacitance of the phase shifter directly affects the energy consumption by the phase modulator in producing a “bit” of data, also known as energy per bit (Miller, 2009, Miller, 2012, Miller et al., 1997). For devices with smaller footprint where the driving electrodes have negligible inductance, the energy per bit directly depends upon the total junction capacitance of the phase shifter. For larger devices, however, the energy consumption must include the energy required for electrode charging, in addition to the phase shifter’s energy consumption.

All in all, modulation efficiency and energy-per-bit are directly proportional to the effective junction capacitance.

For a fixed drive voltage, junction capacitance per unit length and the modulator series resistivity has significant influence over phase shifter's modulation bandwidth. The higher the capacitance, the larger the RC-time constant and lower the bandwidth. To increase bandwidth, the junction capacitance must be reduced which, in turn, means reducing the modulation efficiency. Therefore, a trade-off exists in the design of phase modulator and optimization is necessary.

The third device level FOM is the modulation bandwidth which is perhaps the most important FOM of a phase modulator. It is defined as the frequency at which the modulation is reduced to 50% of the maximum value (Reed et al., 2010). Again, for a device footprint so small that the inductance is negligible, the bandwidth is measured by the RC-time constant of the phase shifter. For larger devices, however, the electrode resistance, capacitance and inductance must be taken in to account.

Optical loss, the fourth and final device level FOM, is the total loss in the optical power due to the cross-sectional dimensions of the waveguide, side-wall roughness, defects in the bulk of the core, and presence of free carriers in the path of optical mode. To achieve higher modulation efficiency and bandwidth, higher dopant density is required which, in turn, increases the optical loss.

### **2.2.2 System Level FOMs**

The system level FOMs pertain to the intensity modulator and include modulation efficiency, extinction ratio, energy consumption and modulation speed (Pantouvaki et al., 2013). At the system level, the modulation efficiency (and so the junction capacitance at the device level) can be translated into modulator footprint, qualitatively. The higher the efficiency, the smaller phase shifter length it takes to

achieve the required phase shift.

The smaller device footprint results in smaller energy-per-bit due to reduced charging energy required by the electrodes. Moreover, for RRM, smaller footprint means that the ring radius can be very small which allows to achieve higher passive resonator bandwidth due to reduced quality factor and resonator-photon lifetime (Bogaerts et al., 2011). The smaller footprint is directly affected by the modulation efficiency. The device level modulation efficiency hence plays a pivotal role in the system level performance of the modulator.

At system level, the modulation speed is measured by the modulator's ability to carry data at a particular rate, typically measured in Giga-bits-per-second (Gbps). Once the modulator bandwidth at system level is known, modulation speed or bit rate may be found for non-return-to-zero (NRZ) bit stream:  $BR \approx 1.5 \times BW$  (Pantouvaki et al., 2013).

Extinction ratio (ER), measured in decibels (dB), is the ratio of the maximum intensity at the output when the modulator is set to send optical '1' ( $I_{max}$ ), to the maximum intensity at the output when the modulator is set to send optical '0' ( $I_{min}$ ). This ratio decides the reach of an optical interconnect and the receiver sensitivity required to demodulate optical signals effectively. For short reach interconnect applications, this ratio should preferably be in the range of 4–5 dB, although  $>7$  dB is highly desirable (Reed et al., 2010). Larger modulation efficiency allows for achieving higher ER in a smaller device and achieving larger interconnect reach.

The quantity relevant for calculation of overall link budget is the insertion loss (IL). Insertion loss is the total optical loss that occurs due to addition of an optical device in a system. The total mode loss difference that occurs with and without an optical modulator is the insertion loss associated with the modulator. This loss includes

the passive mode losses occurring due to waveguide design (radiation loss due to cross-section dimensions and waveguide bend, intermodal and substrate coupling losses etc.) and material loss (bulk and surface scattering loss). The insertion loss may be significant for MZM device, however, RRM devices may be designed to reduce this loss as the active free carrier loaded portion is located on the ring where the mode travels only when an optical ‘0’ is required at the output (Rosenberg et al., 2012). However, MZM devices are more preferable for the higher ER associated with them.

Photonic integrated circuit designed to operate for a particular optical wavelength should operate reasonably well for adjacent wavelengths as well, as the source wavelength can deviate. The range of optical wavelengths (or frequencies) for which the designed device is still operable is the optical bandwidth (OBW) of the device. The OBW of the intensity modulation devices (MZM or RRM) are based on the physical dimensions and the material system of the structure. MZMs are generally more stable in terms of performance over a wide range of optical wavelengths as compared to RRM (Reed Graham et al., 2014). The MZMs offer high OBW (20 – 80 nm) as compared to their narrowband counterparts (RRMs) which offer OBW typically <1 nm (~100 pm) (Reed Graham et al., 2014). Narrowband devices’ yield is significantly low, as compared to wideband MZMs, as they are prone to fabrication tolerances and are highly temperature sensitive where, for example, a nanometre increase in the average ring width changes the resonant frequency by 0.25 nm (Barwicz et al., 2007).

All in all, trade-offs also exist at the system level; MZMs support higher ERs, larger OBW and higher yield but consume more power in electrode charging, result in higher insertion losses and larger footprint. On the other hand, RRM are narrowband, offer low yield, and are temperature sensitive but are high speed, offers low power

consumption, insertion loss and have small footprint. Achieving large ERs in RRAMs and high speed in MZMs require careful phase shifter design optimization. It can be deduce from this section that almost all the system level FOMs are either directly or indirectly influenced by the device level FOMs.

### **2.3 Modulation Mechanisms in Silicon**

Modulation generally implies change in some quantity of interest with respect to change in some other quantity which directly or indirectly influences the quantity of interest. For optical modulation, the quantity of interest is the optical field. The quantities which influence the optical field may include electrical signal (voltage and/or current), temperature and pressure. The parameters of interest in optical field include amplitude, frequency, phase, and polarization of the field. In optical phase and intensity modulation, however, phase of the optical wave is the parameter of interest. The phase of the wave is indirectly modulated by the effective index modulation (see section 2.1). Hence, electrical voltage, current, temperature or pressure should affect the refractive index of the waveguide in order to influence the phase of the optical wave (Reed, 2004). Following, various mechanisms of modulation possible in silicon are described with their merits and shortcomings. In particular, an attempt has been made to present the most viable candidate for high speed modulation in silicon.

#### **2.3.1 Electro-Optic Effects**

Direct modulation of the complex refractive index of a material due to applied electric field is known as the electro-optic (EO) effect. This is the primary and most suitable candidate to achieve modulation in semiconductor devices because of the ultrafast response of the material to the applied fields. The modulation of the real part of the complex refractive index (real index) is known as *electrorefraction* while that of the imaginary part (absorption coefficient) is known as *electroabsorption*.

The linear variation in semiconductor's real refractive index with respect to the applied electric field, known as Pockel effect, is absent in silicon for its highly symmetric (centrosymmetric) structure. Hence, realization of the linear electro-optic effect based modulators is not straightforward in silicon. Methods based on strain-induction in the silicon crystal lattice to break the crystal symmetry have been pursued (Chmielak et al., 2013, Chmielak et al., 2011, Damas et al., 2014, Jacobsen et al., 2006, Schriever et al., 2012, Sharif Azadeh et al., 2015) to achieve Pockel effect and hence linear modulation. However, the quantum of this effect is small (Soref et al., 1987a) and still needs further experimental investigations. Secondly, strain-induction may not always be CMOS-compatible, as other non-compatible materials and processes may also be introduced to achieve strain (Reed et al., 2010, Wen et al., 2016).

The second electrorefraction effect, in which the change in real index of the material is proportional to the square of the applied electric field, is the Kerr effect. This effect is present in silicon but is inherently very low (Osgood et al., 2009), producing a change of the order of  $10^{-4}$  in the real index of lightly doped silicon at the applied electric field of 1 MV/cm (Soref et al., 1987a). This field strength is above the breakdown potential of the lightly doped silicon. Again, strain-engineering has been used to enhance this effect in silicon, however, the materials used to enhance the second-order Kerr effect are not compatible with the CMOS process (Hochberg et al., 2006, Khurgin et al., 2015, Puckett et al., 2014).

The third major electro-optic effect, which is based on electroabsorption, is the Franz-Keldysh effect (FKE). Although FKE affects both the real index and the absorption, however, it is predominantly an electroabsorption effect. Applied electric field distorts the crystal band structure thereby changing the complex refractive index. The bandgap energy shifts due to the applied field and this effect is prominent at the